

Acoustic detection of high-resistance states in gated bilayer graphene devices

Guo-Quan Qin(秦国铨), Yi-Bo Wang(王奕博), Guo-Sheng Lei(雷国盛), Zhuo-Zhi Zhang(张拙之), Xiang-Xiang Song(宋骧骧), and Guo-Ping Guo(郭国平)

Citatio: Chin. Phys. B, 2025, 34 (**9**): 097201. DOI: 10.1088/1674-1056/ade1c6
http://cpb.iphy.ac.cn; http://iopscience.iop.org/cpb

What follows is a list of articles you may be interested in

Valley-dependent transport in a mescoscopic twisted bilayer graphene device

Wen-Xuan Shi(史文萱), Han-Lin Liu(刘翰林), and Jun Wang(汪军)

Chin. Phys. B, 2024, 33 (**1**): 017205. DOI: 10.1088/1674-1056/acf9e4

Emergence of correlations in twisted monolayer-trilayer graphene heterostructures

Zhang Zhou(周璋), Kenji Watanabe, Takashi Taniguchi, Xiao Lin(林晓), Jinhai Mao(毛金海), and Hong-Jun Gao(高鸿钧)

Chin. Phys. B, 2023, 32 (**9**): 097203. DOI: 10.1088/1674-1056/ace3a8

Tunable correlation in twisted monolayer-trilayer graphene

Dongdong Ding(丁冬冬), Ruirui Niu(牛锐锐), Xiangyan Han(韩香岩), Zhuangzhuang Qu(曲壮壮), Zhiyu Wang(王知雨), Zhuoxian Li(李卓贤), Qianling Liu(刘倩伶), Chunrui Han(韩春蕊), and Jianming Lu(路建明)

Chin. Phys. B, 2023, 32 (**6**): 067204. DOI: 10.1088/1674-1056/acc8c3

Correlated states in alternating twisted bilayer-monolayer-monolayer graphene heterostructure

Ruirui Niu(牛锐锐), Xiangyan Han(韩香岩), Zhuangzhuang Qu(曲壮壮), Zhiyu Wang(王知雨), Zhuoxian Li(李卓贤), Qianling Liu(刘倩伶), Chunrui Han(韩春蕊), and Jianming Lu(路建明)

Chin. Phys. B, 2023, 32 (**1**): 017202. DOI: 10.1088/1674-1056/ac9de4

Observation of quadratic magnetoresistance in twisted double bilayer graphene

Yanbang Chu(褚衍邦), Le Liu(刘乐), Yiru Ji(季怡汝), Jinpeng Tian(田金朋), Fanfan Wu(吴帆帆), Jian Tang(汤建), Yalong Yuan(袁亚龙), Yanchong Zhao(赵岩翀), Xiaozhou Zan(昝晓州), Rong Yang(杨蓉), Kenji Watanabe, Takashi Taniguchi, Dongxia Shi(时东霞), Wei Yang(杨威), and Guangyu Zhang(张广宇)

Chin. Phys. B, 2022, 31 (**10**): 107201. DOI: 10.1088/1674-1056/ac6866

RAPID COMMUNICATION

Acoustic detection of high-resistance states in gated bilayer graphene devices

Guo-Quan Qin(秦国铨)[1,2,3], Yi-Bo Wang(王奕博)[1,2,3], Guo-Sheng Lei(雷国盛)[1,2,3], Zhuo-Zhi Zhang(张拙之)[1,2,3], Xiang-Xiang Song(宋骧骧)[1,2,3,†], and Guo-Ping Guo(郭国平)[1,3,4]

[1] *CAS Key Laboratory of Quantum Information, University of Science and Technology of China, Hefei* 230026, *China*
[2] *Suzhou Institute for Advanced Research, University of Science and Technology of China, Suzhou* 215123, *China*
[3] *CAS Center for Excellence in Quantum Information and Quantum Physics, University of Science and Technology of China, Hefei* 230026, *China*
[4] *Origin Quantum Computing Company Limited, Hefei* 230088, *China*

(Received 13 May 2025; revised manuscript received 6 June 2025; accepted manuscript online 6 June 2025)

Applying a perpendicular electric field to bilayer graphene (BLG) induces an electrically tunable bandgap, so that insulating states with resistances exceeding $\sim 10^8$ Ω can be generated. These high-resistance states pinch off the conducting channel, thereby enabling high-quality gated devices for classical and quantum electronics. However, it is challenging to precisely quantify these states electrically due to their high resistances, especially when different areas of the device are operated in different high-resistance states. Here, taking advantage of the strong acoustoelectric effect, we demonstrate the detection of these high-resistance states in a multi-gated BLG device using surface acoustic waves. Under different gating configurations, the device is operated in different high-resistance states. Although these states have similar resistances of $\sim 10^8$ Ω, we show their acoustoelectric responses exhibit pronounced differences, thereby allowing the acoustic detection. More interestingly, we demonstrate that when the conducting channel is pinched off by one top gate, we are still able to acoustically, but not electrically, detect the gating effect of another top gate. Our results reveal the powerful capability and the promising future of acoustically characterizing BLG and other two-dimensional materials, especially their electronic states with high resistances.

Keywords: bilayer graphene, surface acoustic waves, acoustoelectric effects, high-resistance states

PACS: 72.80.Vp, 43.38.Rh, 72.50.+b

DOI: 10.1088/1674-1056/ade1c6 **CSTR:** 32038.14.CPB.ade1c6

1. Introduction

Bilayer graphene (BLG) has attracted significant research interest in electronic applications since a tunable bandgap can be induced by an external perpendicular electric field.[1–4] By tuning the Fermi level of BLG into the bandgap, high-quality insulating states with high resistances above $\sim 10^8$ Ω are generated.[5] These high-resistance states not only can serve as the "OFF" state in classical electronic devices,[6] but also can be employed as tunnel barriers to define quantum dots[7–9] for quantum information processing.[10] However, their high resistances bring technical challenges in precisely identifying and quantifying these states through traditional transport measurements, especially when multiple high-resistance states are electrically connected in series. Therefore, alternative and/or complementary detection strategies are highly desirable.

Surface acoustic waves (SAWs) propagating on the surfaces of piezoelectric substrates can interact with charge carriers in an embedded two-dimensional (2D) electron system,[11–13] leading to the acoustoelectric effect.[14,15] Utilizing this effect, a variety of electrically tunable microwave devices have been developed.[16,17] More importantly, through the acoustoelectric effect, the attenuation and the velocity of SAWs exhibit pronounced responses when varying the conductivity of the charge carriers, offering the possibility of acoustically detecting electronic states.[18–24] Recently, increasing attention has been devoted to acoustoelectric effects in 2D materials.[25–31] This is because 2D materials can be easily transferred onto piezoelectric substrates[27,32–34] to achieve strong acoustoelectric effects due to the nanoscale distances between charge carriers and SAWs. Numerous phenomena have been studied, such as acoustoelectric current,[25,26,30,35–37] negative resistance,[38] valley acoustoelectric effects,[39] and oscillating acoustoelectric effects.[29] Although acoustic measurements of quantum oscillations in graphene[27,40] have been demonstrated very recently, the capability of acoustically detecting high-resistance states in gated devices based on 2D materials remains highly unexplored.

Here, we demonstrate the powerful capability of acoustically detecting high-resistance states in a gated BLG device. The device consists of two sets of interdigital transducers (IDTs) for actuating and detecting SAWs, and a BLG

†Corresponding author. E-mail: songxx90@ustc.edu.cn

© 2025 Chinese Physical Society and IOP Publishing Ltd. All rights, including for text and data mining, AI training, and similar technologies, are reserved.

field-effect transistor (FET) equipped with a back gate and two top gate electrodes. Leveraging the electrically tunable bandgap of BLG, the device is operated in two high-resistance states induced by different top gates. We show that although the resistances of these two states are similar ($\sim 10^8$ Ω), their responses in SAW transmission signals exhibit pronounced differences, enabling sensitive acoustic detection of high-resistance states. More importantly, when the device is pinched off by one top gate so that transport measurements become invalid, the strong acoustoelectric effect still enables acoustically detecting responses upon tuning the other top gate. Our results demonstrate the promising future of investigating high-resistance states in BLG using SAWs, which can be readily extended to characterize the diverse family of 2D materials.

2. Methods

Figure 1(a) shows the optical microscope image of the investigated hybrid device, which consists of two sets of IDTs (only one set is shown in Fig. 1(a)) and a FET fabricated on a piezoelectric substrate of GaAs. The IDTs are fabricated using standard electron beam lithography followed by electron beam evaporation of 35 nm Al. The separation between the two sets of IDTs is 600 μm. The IDTs' electrodes are of the double-electrode type to reduce reflections from the finger electrodes. Both the electrode widths and the center-to-center distances between adjacent electrodes are 400 nm, resulting in the SAW wavelength $\lambda = 3.2$ μm. According to the acoustic velocity $v \sim 2900$ m/s of GaAs, the center frequency of the SAW is expected to be $f \sim 900$ MHz.

Between the two sets of IDTs, we use electron beam lithography and evaporation to fabricate a metal back gate (BG, Ti/Pd = 3/20 nm). Subsequently, we transfer a sandwiched heterostructure onto BG using the well-established "pick-up" transfer method.[32,33] The heterostructure is stacked by encapsulating a BLG sheet with two hexagonal boron nitride (hBN) flakes. All flakes are prepared by mechanical exfoliation. After the transfer process, the heterostructure is etched to expose the edges of BLG for electrical contact.[32] Finally, a layer of Cr/Au = 5/50 nm is deposited onto the heterostructure to form the source (S), the drain (D) and two top gate electrodes (TG1 and TG2), respectively. The two top gates are of different widths (2 μm for TG1, and 1 μm for TG2). The optical microscope image and the cross-sectional schematic of the FET are shown in Figs. 1(b) and 1(c), respectively. The three gate electrodes divide the BLG flake into three parts: 1) the dual-gated region between BG and TG1 (referred to as DG1 area for simplicity), 2) the dual-gated region between BG and TG2 (referred to as DG2 area), and 3) the single-gated region which is not covered by any top gate (referred to as BG area).

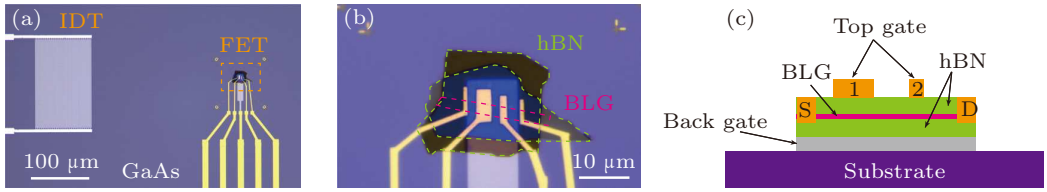


Fig. 1. The structure of our device. (a) Optical microscope image of the device, showing one set of IDTs and a FET fabricated on a piezoelectric substrate of GaAs. (b) Zoom-in of the FET region highlighted by the orange dashed box in (a). The green and pink dashed lines mark the edges of the hBN and BLG flakes, respectively. (c) Cross-sectional schematic of the FET. The hBN (green) and BLG (pink) flakes are stacked as a sandwiched heterostructure, which is placed on top of a metal back gate (gray). Two top gates (orange) with different widths, labeled as 1 and 2, respectively, are deposited above the heterostructure. The source (S, orange) and drain (D, orange) are used for transport measurements.

3. Results and discussion

The device is characterized in a He-3 refrigerator with a base temperature of ~ 350 mK. First, we measure the transport properties of the FET using lock-in techniques under an AC source-drain bias of $V_{\rm SD} = 100$ μV at 17.7 Hz. Figure 2(a) shows the measured differential conductance $\mathrm{d}I/\mathrm{d}V_{\rm SD}$ when varying voltages applied to BG ($V_{\rm BG}$) and TG1 ($V_{\rm TG1}$). Two crossing dark blue lines are visible, where $\mathrm{d}I/\mathrm{d}V_{\rm SD}$ reaches a minimum. The horizontal line corresponds to the charge neutrality point (CNP) of the BG area, and the diagonal line represents the CNP of the DG1 area where a bandgap is induced by the perpendicular electric field generated by gate voltages.[1,2,5,6]

Next, we focus on the DG1 area. Using a simple parallel-plate capacitor model, the electric field D and the charge density n in the DG1 area are described as[1]

$$D = \varepsilon_{\rm hBN}\left(V_{\rm BG} - V_{\rm BG}^0\right)/(2d_{\rm b}) - \varepsilon_{\rm hBN}\left(V_{\rm TG1} - V_{\rm TG1}^0\right)/(2d_{\rm t}), \quad (1)$$

$$n = \left[\varepsilon_{\rm hBN}\left(V_{\rm BG} - V_{\rm BG}^0\right)/(2d_{\rm b}) + \varepsilon_{\rm hBN}\left(V_{\rm TG1} - V_{\rm TG1}^0\right)/(2d_{\rm t})\right]/e. \quad (2)$$

Here, e is the electron charge, $\varepsilon_{\rm hBN}$ is the dielectric constant of hBN, $d_{\rm b}$ and $d_{\rm t}$ are the thicknesses of the bottom and the top hBN flakes, respectively, and $V_{\rm BG}^0$ and $V_{\rm TG1}^0$ are the voltage offsets of BG and TG1, respectively, which originate from unintentional doping induced in the fabrication process.[1] Setting $n = 0$, we estimate the slope of the diagonal line as $-d_{\rm t}/d_{\rm b} \sim 0.59$ (calculated based on the thicknesses of hBN flakes mea-

sured by the atomic force microscopy), which is comparable with the value of ~ 0.57 extracted from Fig. 2(a). Therefore, according to Eqs. (1) and (2), along the diagonal line, as $V_{\rm BG}$ and $V_{\rm TG1}$ change toward the top-left or bottom-right corner, the electric field $|D|$ at the DG1 area increases while the Fermi level of BLG in the DG1 area is always kept in the bandgap.[41] We would like to point out that the diagonal line gradually broadens upon increasing $|D|$. This phenomenon originates from the increased bandgap,[1,2,5,6] which is consistent with previous reports.[2,3,5,6,42] When varying $V_{\rm BG}$ and $V_{\rm TG2}$, similar features are observed, as shown in Fig. 2(b).

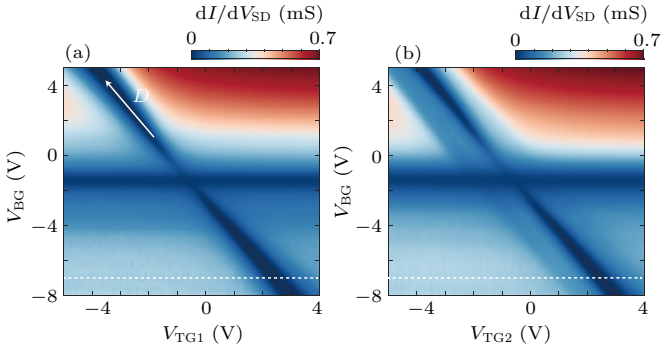


Fig. 2. Transport measurements. (a) Differential conductance dI/d$V_{\rm SD}$ of the FET as a function of $V_{\rm BG}$ and $V_{\rm TG1}$. Considering the voltage offset of $V^0_{\rm TG2}$, here $V_{\rm TG2} = V^0_{\rm TG2} = -0.66$ V. The white arrow indicates the direction at which the electric field D increases. (b) dI/d$V_{\rm SD}$ as a function of $V_{\rm BG}$ and $V_{\rm TG2}$, at $V_{\rm TG1} = V^0_{\rm TG1} = -0.70$ V. White dashed lines mark the positions where Fig. 3 is obtained.

To further study the electrical tuning effect of different top gates, we extract dI/d$V_{\rm SD}$ as functions of voltages applied to TG1 ($V_{\rm TG1}$) and TG2 ($V_{\rm TG2}$), respectively, at a fixed $V_{\rm BG} = -7$ V (the white dashed lines in Fig. 2). As shown in Fig. 3(a), the red (blue) curve approaches zero where the DG1 (DG2) area is tuned to the CNP, and increases sharply as $V_{\rm TG1}$ ($V_{\rm TG2}$) moves away from the CNP. This is better evidenced in differential resistances shown in Fig. 3(b). It is clear that either tuning $V_{\rm TG1}$ or $V_{\rm TG2}$ switches the device from conductive ($\sim 10^3$ Ω) to high-resistance ($\sim 10^8$ Ω) states, suggesting high-quality bandgap formations in both DG1 and DG2 areas. It is worth noting that the maximum differential resistances of these two states are nearly identical, according to the transport measurements. We would like to point out that a slight difference in peak broadening is observed in Fig. 3(b), which can be understood from the view of different widths of the corresponding top gate electrodes. Given the presence of inhomogeneities and impurities in real devices,[5] hopping via disorder traps near the band edge leads to leakage. A wider top gate (TG1) tends to suppress this leakage by creating a wider insulating region.

After transport measurements, we use the vector network analyzer to detect the SAW transmission signals while varying $V_{\rm TG1}$ and $V_{\rm TG2}$, respectively. Here we choose the third harmonic mode of the SAW ($f = 2.713$ GHz) since its corresponding wavelength (~ 1 μm) is comparable with the widths of both top gate electrodes. As shown in Fig. 3(c) (Fig. 3(d)), the phases ϕ (the amplitudes $|S_{21}|$) of the SAW transmission signals exhibit pronounced responses upon tuning $V_{\rm TG1}$ and $V_{\rm TG2}$ to approach the CNP, respectively. Varying $V_{\rm BG}$ results in similar responses of ϕ and $|S_{21}|$ as well (insets of Figs. 3(c) and 3(d)).

The mechanism behind the acoustic detection of electronic states is due to the interaction between SAWs and charge carriers in BLG. The propagation of SAWs generates an accompanying piezoelectric field through the piezoelectric effect. The in-plane piezoelectric component acts on charge carriers, resulting in their directional and oscillatory motions.[29] Meanwhile, the screening field induced by charge carriers combines with the piezoelectric field, forming an effective electric field that modifies the propagation of SAWs via the inverse piezoelectric effect.[12] Such an interaction transfers energies between SAWs and charge carriers, and can be described by a simple relaxation model[27] as

$$\frac{\delta v}{v} - \frac{{\rm i}\Gamma}{k} = \frac{K^2_{\rm eff}}{2}\frac{1}{1+{\rm i}\sigma_{xx}/\sigma_{\rm m}}. \tag{3}$$

Here, v is the acoustic velocity, δv is the velocity shift, Γ is the SAW attenuation coefficient, k is the SAW wave vector, σ_{xx} is the sheet conductivity of BLG, $K^2_{\rm eff}$ and $\sigma_{\rm m}$ are the electromechanical coupling efficiency and the characteristic sheet conductivity of the piezoelectric substrate, respectively. Therefore, δv (Γ) determines the phase ϕ (the amplitude $|S_{21}|$) of the SAW. The inset of Fig. 3(b) shows the calculated $\delta v/v$ and Γ based on Eq. (3), which are nonlinearly scaled with σ_{xx}. In our experiment, $\sigma_{\rm m}$ is expected to be $\sim 10^{-7}$ S for GaAs.[12] Since σ_{xx} can be tuned from $\sim 10^{-4}$ S to $\sim 10^{-8}$ S upon gating, we are able to observe pronounced responses in the SAW transmission signals near the CNP. Note that as σ_{xx} decreases, $\delta v/v$ increases monotonically while Γ exhibits a non-monotonic behavior (inset of Fig. 3(b)). However, as shown in Fig. 3(d), $|S_{21}|$ also exhibits a dip in our experiments, which may result from the relatively large power of SAWs.[11]

More interestingly, as shown in Figs. 3(c) and 3(d), the blue and the red curves exhibit distinct differences near the CNP for both ϕ and $|S_{21}|$. This demonstrates that the small conductivity difference between the two high-resistance states, which is not visible in the electrical measurements, becomes detectable after being transduced to acoustic signals. However, this transducing mechanism cannot be quantitatively understood at present. According to the relaxation model,[27] the detected acoustic signals should be proportional to the area of the corresponding dual-gated region upon tuning $V_{\rm TG1(2)}$. Therefore, it is expected that the acoustic responses upon varying $V_{\rm TG1}$ should be more pronounced, compared with varying $V_{\rm TG2}$. However, as shown in Figs. 3(c) and 3(d), $|S_{21}|$ follows this trend, while ϕ demonstrates the opposite behavior. This

hints at possible new mechanisms beyond the simple relaxation model, in which further knowledge of the impedance at different parts of the device may be needed to account for the transmission/reflection at their interfaces. Nevertheless, our finding suggests that high-resistance states formed in DG1 and DG2 areas can be acoustically distinguished, even though their resistances are found to be nearly identical around $\sim 10^{-8}$ S from traditional transport measurements.

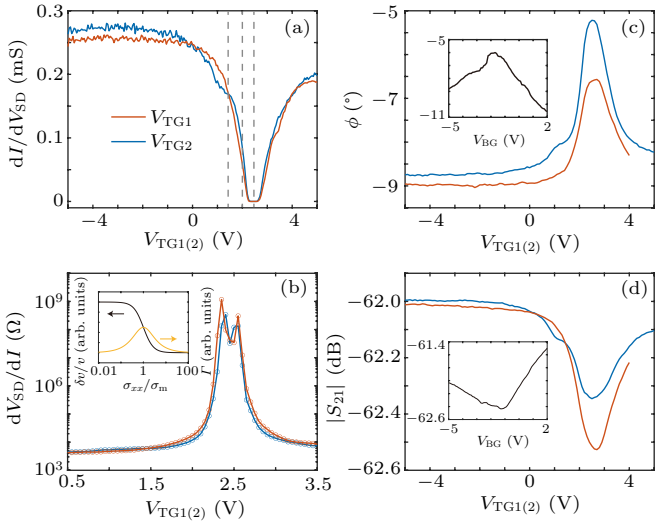


Fig. 3. Electrical and acoustic responses of the FET. (a) Differential conductance curves as functions of V_{TG1} (red) and V_{TG2} (blue) at $V_{BG} = -7$ V, respectively, which are extracted from the white dashed lines in Fig. 2. (b) Differential resistance curves as functions of V_{TG1} (red) and V_{TG2} (blue), respectively, which are calculated from the data in (a). Inset shows calculated $\delta v/v$ and Γ as a function of σ_{xx}/σ_m based on Eq. (3). (c) Phase ϕ and (d) amplitude $|S_{21}|$ responses of the SAW transmission signals as functions of V_{TG1} (red) and V_{TG2} (blue), respectively, which are obtained at the voltage configuration in (a). Insets of (c) and (d) show ϕ and $|S_{21}|$ as a function of V_{BG}, respectively. Here $V_{TG1} = V^0_{TG1}$ and $V_{TG2} = V^0_{TG2}$. Gray dashed lines in (a) mark the positions where Fig. 4 is obtained.

To further demonstrate the capability of acoustically detecting high-resistance states, we simultaneously use both top gates for electrical tuning. Figure 4(a) shows the measured dI/dV_{SD} as a function of V_{TG1} at different V_{TG2} (corresponding to the gray dashed lines in Fig. 3(a)). When $V_{TG2} = 1.4$ V and 2.0 V, a clear tuning trend of dI/dV_{SD} with V_{TG1} is observed, which is similar to Fig. 3(a). However, when $V_{TG2} = 2.5$ V, the DG2 area is tuned to the high-resistance state (the rightmost gray dashed line in Fig. 3(a)), thereby pinching off the conducting channel. Since DG1 and DG2 areas are connected in series, the overall dI/dV_{SD} already approaches zero and cannot further respond to electrical tuning on the DG1 area with V_{TG1}. This is more clearly evidenced in the differential resistance plot shown in Fig. 4(b).

In sharp contrast, the propagation of SAWs is not pinched off upon gating, so that SAWs can interact with charge carriers in different BLG areas along their propagation. Therefore, as shown in Figs. 4(c) and 4(d), both ϕ and $|S_{21}|$ of the SAW transmission signals respond to V_{TG1}, regardless of the states in the DG2 area set by V_{TG2}.

The acoustic detection scenario and its difference with respect to traditional transport measurements are summarized in Fig. 5. Manipulating DG1 and DG2 in either high-resistance or conductive states results in four possible cases, labeled as (i) to (iv). Since high-quality high-resistance states can be achieved in both DG1 and DG2 areas and are connected in series, traditional transport measurements only detect whether the conducting channel is pinched off, thus failing to distinguish cases (ii), (iii), and (iv). However, the acoustic detection not only enables identification of high-resistance states underneath different top gates with different widths (between cases (ii) and (iii), see Fig. 3), but also responds differently upon gating even when the conducting channel is already pinched off by another top gate (between cases (ii) and (iv), see Fig. 4).

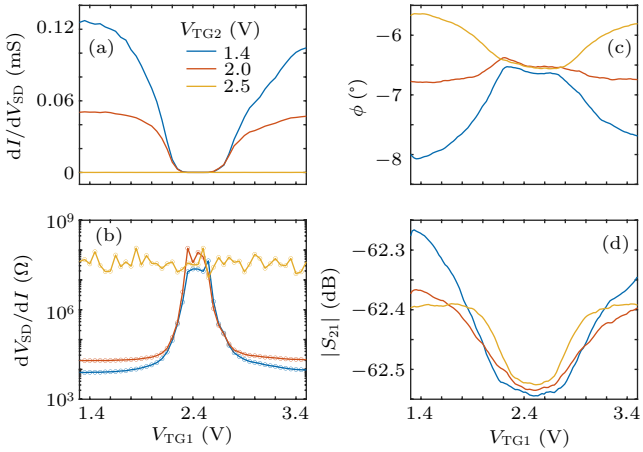


Fig. 4. Electrical and acoustic responses of the FET under a combined tuning of both top gates. (a) Differential conductance and (b) differential resistance as a function of V_{TG1} at $V_{BG} = -7$ V and $V_{TG2} = 1.4$ V (blue), 2.0 V (red) and 2.5 V (yellow), respectively. (c) Phase ϕ and (d) amplitude $|S_{21}|$ of the SAW transmission signals, obtained at the voltage configuration in (a).

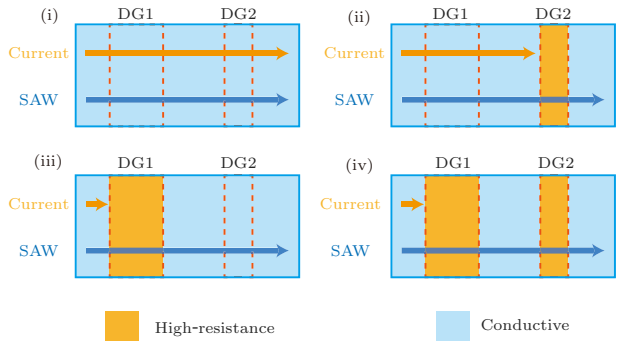


Fig. 5. Possible cases of the device upon gating DG1 and DG2 areas in high-resistance (orange) or conductive (blue) states. Orange and blue arrows represent the electrical current and the propagation of SAWs, respectively, demonstrating the differences between electrical and acoustic detection scenarios.

Our results demonstrate that even when the device's resistance is as large as $\sim 10^8$ Ω, it is still able to acoustically detect its internal electrical properties via the acoustoelectric effect. This is of particular interest to employ SAWs to characterize 2D materials whose Ohmic contacts are difficult to realize, especially under low source–drain bias voltages at low temperature.[43] In addition, the demonstrated acoustic

detection scenario offers possibilities to reveal different, but simultaneously existing, novel insulating electronic states in 2D materials,[44–46] which may be hidden in traditional transport measurements. Moreover, from the quantum information point of view, the high-resistance states are essential for serving as tunnel barriers to define quantum dots.[7–9,47,48] When quantum dots are tuned into a few-electron regime,[49–52] direct transport measurements may be challenging due to the suppressed tunneling rates.[53,54] In such a case, the acoustic detection via SAWs provides an alternative probing scheme.

4. Summary

In conclusion, we fabricate a hybrid device consisting of a multi-gated BLG-based FET and two sets of IDTs for actuating and detecting SAWs. Through comparisons of transport measurement results and acoustically probed signals, we demonstrate that SAW transmission signals are sensitive in detecting high-resistance states, even when their resistances are too large to be distinguished from traditional transport measurements. We further show that when the FET is pinched off by one top gate, the measured SAW transmission signals are able to reflect variations in the conductivity of BLG underneath another top gate. Our results demonstrate the powerful capability and the promising future of employing acoustic detection as an alternative and/or complementary detection strategy beyond traditional transport measurements for characterizing 2D materials.

Acknowledgements

Project supported by the Natural Science Foundation of Jiangsu Province (Grant No. BK20240123), the National Key Research and Development Program of China (Grant No. 2022YFA1405900), and the National Natural Science Foundation of China (Grant Nos. 12274397, 12274401, and 12034018).

References

[1] Zhang Y, Tang T T, Girit C, *et al*. 2009 *Nature* **459** 820
[2] Taychatanapat T and Jarillo-Herrero P 2010 *Phys. Rev. Lett.* **105** 166601
[3] Varlet A, Liu M H, Krueckl V, *et al*. 2014 *Phys. Rev. Lett.* **113** 116601
[4] Oostinga J. B, Heersche H B, Liu X, *et al*. 2008 *Nat. Mater.* **7** 151
[5] Icking E, Banszerus L, Wörtche F, *et al*. 2022 *Adv. Electron. Mater.* **8** 2200510
[6] Icking E, Emmerich D, Watanabe K, *et al*. 2024 *Nano Lett.* **24** 11454
[7] Tong C, Garreis R, Knothe A, *et al*. 2021 *Nano Lett.* **21** 1068
[8] Banszerus L, Rothstein A, Fabian T, *et al*. 2020 *Nano Lett.* **20** 7709
[9] Tong C, Kurzmann A, Garreis R, *et al*. 2022 *Phys. Rev. Lett.* **128** 067702
[10] Jing F M, Zhang Z Z, Qin G Q, *et al*. 2022 *Adv. Quantum Technol.* **5** 2100162
[11] Wixforth A, Kotthaus J P and Weimann G 1986 *Phys. Rev. Lett.* **56** 2104
[12] Wixforth A, Scriba J, Wassermeier M, *et al*. 1989 *Phys. Rev. B* **40** 7874
[13] Efros A L and Galperin Y M 1990 *Phys. Rev. Lett.* **64** 1959
[14] Parmenter R H 1953 *Phys. Rev.* **89** 990
[15] Rotter M, Wixforth A, Ruile W, *et al*. 1998 *Appl. Phys. Lett.* **73** 2128
[16] Hackett L, Miller M, Brimigion F, *et al*. 2021 *Nat. Commun.* **12** 2769
[17] Hackett L, Miller M, Weatherred S, *et al*. 2023 *Nat. Electron.* **6** 76
[18] Wu M, Liu X, Wang R, *et al*. 2024 *Phys. Rev. Lett.* **132** 076501
[19] Friess B, Peng Y, Rosenow B, *et al*. 2017 *Nat. Phys.* **13** 1124
[20] Paalanen M A, Willett R L, Littlewood P B, *et al*. 1992 *Phys. Rev. B* **45** 11342
[21] Willett R L, West K W and Pfeiffer L N 2002 *Phys. Rev. Lett.* **88** 066801
[22] Wang J, Pfeiffer L. N, West K W, *et al*. 2020 *Phys. Rev. B* **101** 165413
[23] Friess B, Umansky V, von Klitzing K and Smet J H 2018 *Phys. Rev. Lett.* **120** 137603
[24] Friess B, Dmitriev I A, Umansky V, *et al*. 2020 *Phys. Rev. Lett.* **124** 117601
[25] Preciado E, Schülein F J R, Nguyen A E, *et al*. 2015 *Nat. Commun.* **6** 8593
[26] Miseikis V, Cunningham J E, Saeed K, *et al*. 2012 *Appl. Phys. Lett.* **100** 133105
[27] Fang Y, Xu Y, Kang K, *et al*. 2023 *Phys. Rev. Lett.* **130** 246201
[28] Nie X, Wu X, Wang Y, *et al*. 2023 *Nanoscale Horizons* **8** 158
[29] Mou Y, Wang J, Chen H, *et al*. 2025 *Phys. Rev. Lett.* **134** 096301
[30] Zhao P, Sharma C H, Liang R, *et al*. 2022 *Phys. Rev. Lett.* **128** 256601
[31] Mou Y, Liu Q, Liu J, *et al*. 2025 *Nano Lett.* **25** 4029
[32] Wang L, Meric I, Huang P Y, *et al*. 2013 *Science* **342** 614
[33] Purdie D. G, Pugno N M, Taniguchi T, *et al*. 2018 *Nat. Commun.* **9** 5387
[34] Pizzocchero F, Gammelgaard L, Jessen B S, *et al*. 2016 *Nat. Commun.* **7** 11894
[35] Zheng S, Zhang H, Feng Z, *et al*. 2016 *Appl. Phys. Lett.* **109** 183110
[36] Tang C C, Chen Y F, Ling D. C, *et al*. 2017 *J. Appl. Phys.* **121** 124505
[37] Liou Y. T, Hernández-Mínguez A, Herfort J, *et al*. 2017 *J. Phys. D: Appl. Phys.* **50** 464008
[38] Yokoi M, Fujiwara S, Kawamura T, *et al.* 2020 *Sci. Adv.* **6** eaba1377
[39] Kalameitsev A V, Kovalev V M and Savenko I G 2019 *Phys. Rev. Lett.* **122** 256801
[40] Mou Y, Chen H, Liu J, *et al*. 2024 *Nano Lett.* **24** 4625
[41] McCann E and Koshino M 2013 *Rep. Prog. Phys.* **76** 056503
[42] Du R, Liu M H, Mohrmann J, *et al*. 2018 *Phys. Rev. Lett.* **121** 127706
[43] Allain A, Kang J, Banerjee K and Kis A 2015 *Nat. Mater.* **14** 1195
[44] Seiler A. M, Geisenhof F. R, Winterer F, *et al*. 2022 *Nature* **608** 298
[45] Liu K, Zheng J, Sha Y, *et al*. 2024 *Nat. Nanotechnol.* **19** 188
[46] Han T, Lu Z, Scuri G, *et al*. 2024 *Nat. Nanotechnol.* **19** 181
[47] Jing F M, Qin G Q, Zhang Z Z, *et al*. 2023 *Appl. Phys. Lett.* **123** 184001
[48] Song X X, Liu D, Mosallanejad V, *et al*. 2015 *Nanoscale* **7** 16867
[49] Banszerus L, Möller S, Hecker K, *et al*. 2023 *Nature* **618** 51
[50] Qin G Q, Jing F M, Hao T Y, *et al*. 2025 *Phys. Rev. Lett.* **134** 036301
[51] Eich M, Herman F, Pisoni R, *et al*. 2018 *Phys. Rev. X* **8** 031023
[52] Jing F M, Shen Z X, Qin G Q, *et al*. 2025 *Phys. Rev. Applied* **23** 044053
[53] Garreis R, Tong C, Terle J, *et al*. 2024 *Nat. Phys.* **20** 428
[54] Denisov A O, Reckova V, Cances S, *et al*. 2025 *Nat. Nanotechnol.* **20** 494